Enhanced relativistic-electron beam energy loss in warm-dense aluminum

X. Vaisseau,[1] A. Debayle,[2,3,4] J.J. Honrubia,[2] S. Hulin,[1] A. Morace,[5] Ph. Nicolaï,[1] H. Sawada,[5] B. Vauzour,[1] D. Batani,[1] F.N. Beg,[5] J.R. Davies,[6] R. Fedosejevs,[7] R.J. Gray,[8] G.E. Kemp,[9] S. Kerr,[7] K. Li,[10] A. Link,[11] P. McKenna,[8] H.S. McLean,[11] M. Mo,[7] P.K. Patel,[11] J. Park,[11] J. Peebles,[5] Y.J. Rhee,[12] A. Sorokovikova,[5] V.T. Tikhonchuk,[1] L. Volpe,[1] M. Wei,[13] and J.J. Santos[1,*]

[1] *Univ. Bordeaux, CNRS, CEA, CELIA (Centre Lasers Intenses et Applications), UMR 5107, F-33405 Talence, France*
[2] *ETSI Aeronáuticos, Universidad Politécnica de Madrid, Madrid, Spain*
[3] *CEA, DAM, DIF, F-91297 Arpajon, France*
[4] *LRC MESO, Ecole Normale Supérieure de Cachan - CMLA, 94235 Cachan, France*
[5] *University of California, San Diego, La Jolla, California 92093, USA*
[6] *Fusion Science Center for Extreme States of Matter, Laboratory for Laser Energetics, University of Rochester, Rochester, New York 14623, USA*
[7] *Department of Electrical Engineering, University of Alberta, Edmonton T6G 2G7, Canada*
[8] *SUPA, Department of Physics, University of Strathclyde, Glasgow G4 0NG, United Kingdom*
[9] *Physics Department, The Ohio State University, Columbus, Ohio 43210, USA*
[10] *GoLP, Instituto de Plasmas e Fusão Nuclear, Instituto Superior Técnico, 1049-001 Lisboa, Portugal*
[11] *Lawrence Livermore National Laboratory, Livermore, California 94550, USA*
[12] *Korea Atomic Energy Research Institute (KAERI), Daejon 305-600, South Korea*
[13] *General Atomics, San Diego, California 92121, USA*

(Dated: December 1, 2014)

Energy loss of relativistic electron beams in warm-dense aluminum is measured in the regime of ultra-high electron beam current density over 2×10^{11} A/cm^2 (time-averaged). The samples are heated by shock compression. Comparing to undriven cold-solid ones, the roles of the different initial resistivity and of the transient resistivity (upon target heating during electron transport) are directly highlighted by the experimental data, reproduced by a comprehensive set of simulations, describing the hydrodynamics of the shock compression, and electron beam generation and transport. We measured a 16% increase in electron resistive energy loss in warm-dense compared to cold-solid samples of identical areal mass.

PACS numbers:

Ultra-high intensity laser interactions with dense targets stand out as the best way to produce high-current relativistic electron beams (REB). This regime of electron sources gave rise to a multitude of applications this past decade, such as ion beam production, coherent and incoherent XUV and X-ray emission, and isochoric heating of solid targets to extreme temperatures. The electron-driven fast ignition (FI) scenario in inertial confinement fusion (ICF) [1] is one of the potential application areas of such beams. In this scheme, DT fusion is to be ignited by a REB generated by an intense pulse ($\sim 10^{20}$ W.cm^{-2}, ~ 100 kJ, ~ 10 ps) interacting with the inner tip of a cone [2], re-entrant to a compressed DT pellet, at stagnation. The electrons should have a mean energy of $1 \leq \bar{\varepsilon}_h \leq 2$ MeV adapted for an efficient energy deposition in the ≈ 1 g/cm^2 areal density core. Only 20 kJ need to be deposited in the core to trigger the reactions [3]. Yet, despite these seemingly achievable criteria, a large controversy exists in the community concerning the initial laser intensity required to generate the REB [2, 4–8]. To bring that energy to the core, and assess FI feasibility, it is fundamental to understand the REB transport, at current densities $j_h > 10^{11}$ A.cm^{-2}, through warm moderate over-dense, and highly resistive plasma, representative of regions near the cone tip.

Electron beam energy losses incident into a material are commonly associated with inelastic collisions with bound and free electrons, and plasma waves [9]. These processes, well documented and described in textbooks, are however insufficient at the extremely high j_h, achieved in relativistic laser-plasma experiments, where resistive losses induced by the neutralizing return current, of density $\boldsymbol{j_e}$, become important. Indeed, while the time rate of collisional energy loss by the electron beam per unit volume is $\dot{W}_{\rm coll} \propto \rho j_h$, with ρ the material density, by assuming a perfect current neutralization $\boldsymbol{j_e} = -\boldsymbol{j_h}$, the rate for the resistive energy loss is $\dot{W}_{\rm res} \simeq \eta j_h^2$, with η the material resistivity. This last process, predicted theoretically [10] and by numerical simulations [11], has been recently experimentally evidenced in well-controlled cold-solid targets [12, 13] - a feature not yet observed in the warm dense matter regime. This lack of data is not only due to the small number of experiments but also to the transient nature of the process and the necessity of systematic, and often indirect measurements of the electron beam and target parameters. Besides, a hierarchy of codes is required to assess the relevant observables.

This letter presents the first measurements of resistive energy loss of a relativistic electron beam in warm-dense matter for current density up to $\bar{j}_h \approx 2 \times 10^{11}$ A.cm^{-2}.

* santos.joao@celia.u-bordeaux1.fr

The resistive energy losses were unraveled by comparatively characterizing REB transport in cold-solid and in warm-compressed aluminum (Al) samples of identical areal density (ρL). Al was chosen for being the best modeled material in the warm dense matter state [15]. The Al warm samples, obtained by ns laser-generated planar shock-compression, reached a density of $\rho \sim 5.4\,\mathrm{g/cc}$ with a temperature of $T \sim 3\,\mathrm{eV}$ behind the shock front, close to the material Fermi temperature. In these conditions, the resistivity is predicted to rise by a factor of >15 compared to its cold-solid state value [14, 15], and to produce a significant increase of the REB resistive losses in warm samples. As the areal density ρL is kept constant during the compression, the REB collisional energy losses remain invariant while the resistive losses change. The REB transport efficiency shows a clear dependence on the sample state, with a significant contribution from resistive losses, peaking at the same level as collisional losses in the Al compressed-warm targets. Benchmarked simulations provide a detailed description of the transient behavior of the Al resistivity upon REB-induced heating.

The experiment was carried out at the Lawrence Livermore National Laboratory (USA) on the JLF-Titan laser facility, using a dual laser beam configuration. Samples were shock-compressed by a long pulse beam (LP) on the rear surface. At a chosen delay, the target front surface was irradiated by a short pulse beam (SP) generating the REB propagating against the shock. The $\lambda_{\mathrm{SP}} = 1.06\,\mu\mathrm{m}$, $\tau_{\mathrm{SP}} = 0.7\,\mathrm{ps}$ full-width-at-half-maximum (FWHM) SP was focused to a Gaussian-like spot of $7\,\mu\mathrm{m}$ diameter (FWHM), containing 40% of the on-target $115 \pm 30\,\mathrm{J}$ laser energy and yielding a $(2 \pm 1) \times 10^{20}\,\mathrm{W.cm^{-2}}$ peak intensity. The SP pedestal intensity contrast due to the amplified spontaneous emission (ASE) was measured to be $\sim 10^{-7}$, 3 ns before the main pulse arrival [16, 17]. The frequency doubled LP ($\lambda_{\mathrm{LP}} = 0.53\,\mu\mathrm{m}$), with a 5 ns square temporal profile and an on-target energy of $410 \pm 9\,\mathrm{J}$ was focused onto a $875\,\mu\mathrm{m}$ FWHM flat top spot by means of a phase zone plate, yielding an intensity of $(1.4 \pm 0.3) \times 10^{13}\,\mathrm{W.cm^{-2}}$. It generated homogeneous shock fronts ensuring planar compression over a radius much greater than the REB radius. The given uncertainties are the standard deviations over the full set of laser shots. The $5 \times 5\,\mathrm{mm^2}$ surface multi-layer foil targets were composed of Al[$5\,\mu$m] - Ag[$5\,\mu$m] - Al[L_0] - Sn[$10\,\mu$m] - Cu[$10\,\mu$m] - PP[$15\,\mu$m], where the central Al layer of variable thickness ($L_0 = \{20, 40, 60, 80\}\,\mu\mathrm{m}$) is called Al-sample, and a rear-side polypropylene (PP) layer used as an ablator. The K-shell ionization fluorescence layers of Ag, Sn and Cu were used to characterize the fast electron source at the front side and at the rear of the Al-sample. The delay between the laser pulses was set according to the desired Al-sample state. For cold-solid Al, a shorter delay was used, allowing the formation of a long plasma, preventing the fast electron from recirculating after their first transit through the K-shell tracers and the Al-sample. In this configuration, the shock reaches the Sn - Al-sample interface without compressing the latter. For the warm-dense Al, a longer delay was used, adjusted according to L_0 and sufficient to allow the shock to cross and practically fully compress the Al-samples. The delays were determined by simulations of the shock formation and propagation, performed with the 2D radiative-hydrodynamic code CHIC [18] and benchmarked by streaked measurements of the optical emission caused by the shock breakout on the targets front side. The two delay categories allowed respectively to study REB transport in cold-solid Al ($T_e = 0.03\,\mathrm{eV}$, $\rho_0 = 2.7\,\mathrm{g/cc}$) and in warm-dense Al ($T_e \sim 3\,\mathrm{eV}$ and $\rho \sim 2\ \rho_0$, behind the shock front) as illustrated in the axial profiles in Fig. 3-a).

The REB radial dispersion against target thickness was inferred from Cu-K_α imaging with both a spherically bent crystal imager [19] and a Kirkpatrick-Baez microscope [20], yielding consistent results. The divergence of the beam, defined by the rate of increase in measured spot size versus distance, i.e. the slope of the beam edge, was measured to be 19° half-angle, independently of the sample state. Fast electron energy loss in the Al-samples was evaluated from the ratio of Sn-K_α to Ag-K_α yield, using an absolutely calibrated Cauchois-type hard X-ray transmission spectrometer [21]. Fig. 1-a) shows the data as a function of the Al-sample areal density (full symbols) for (a) the absolute Sn-K_α yield and (b) the Sn-K_α/Ag-K_α ratio. The former presents variations due to the inherent shot-to-shot fluctuations of the laser parameters, while the latter allows to decorrelate the data from them, and is roughly proportional to the fraction of the fast electrons transmitted by the Al-sample. In the case of warm samples, the ratio has a steeper decrease against ρL compared to the solid samples, showing a clear difference for the thicker targets ($\rho L \geqslant 15.5\ \mathrm{mg.cm^{-2}}$). This behavior is the main signature of extra, non-collisional, energy losses in the warm samples.

To further understand the physics at play and to estimate the electron stopping cross section, the data were compared to integrated simulations. The REB source was computed with the 2D particle-in-cell (PIC) code LSP [22] modeling the SP laser interaction with a $200 \times 200\,\mu\mathrm{m^2}$ Al layer. The ASE-induced pre-plasma exponential density profile, with a scale length set to $50\,\mu\mathrm{m}$, was measured in a previous experiment [16, 17]. The SP temporal profile was a 700 fs FWHM Gaussian with a peak intensity of $10^{20}\,\mathrm{W.cm^{-2}}$. The different REB source characteristics were extracted at $5\,\mu\mathrm{m}$ depth into the target, with the 0-position corresponding to the initial solid-vacuum interface. The REB energy distribution [gray curve on Fig. 2-a)] was averaged over the 2.4 ps duration of the simulation and is well described over the $0.05 \leq \varepsilon_h \leq 140\,\mathrm{MeV}$ energy range by the following normalized analytical expression:

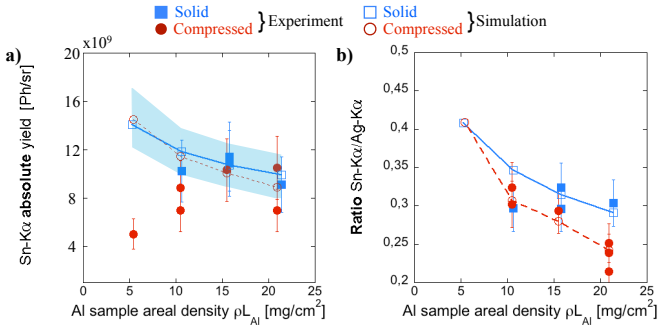

FIG. 1. (color online) **(a)** Measured (full symbols) and simulated (empty symbols) absolute Sn-K$_\alpha$ yields as a function of the Al-sample areal density. Simulation results obtained with $\eta_{\text{laser}\to\text{e}} = 25\%$ (the shaded area corresponds to $\pm 5\%$ variations). **(b)** Measured and simulated Sn-K$_\alpha$/Ag-K$_\alpha$ ratio as a function of the Al-sample areal density.

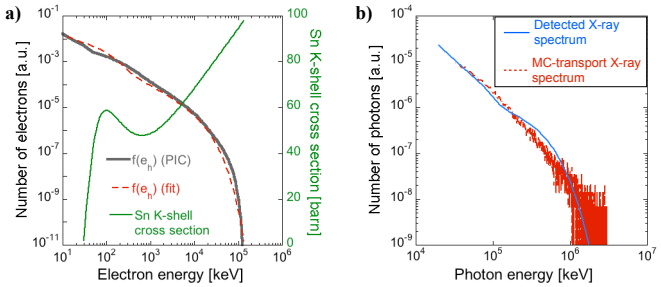

FIG. 2. (color online) **a)** REB spectrum obtained from the PIC simulations (solid grey line) and its analytical fit (Eq. 1, dashed red line) injected into hybrid transport simulations. The Sn tracer K-shell ionization cross section is also represented (solid green line). **b)** Bremsstrahlung spectra results from the MC simulations: experimental spectrum deduced from matching the X-ray detection simulation to the dosimeter layer data (first step: blue solid line) compared to the spectrum generated during the fast electron propagation through the target (second step: dashed red line).

$$f(\varepsilon_h) = \exp\left(-\frac{\varepsilon_h}{T_{h_1}}\right) + \left(\frac{\varepsilon_0}{\varepsilon_h}\right)^{\alpha} \exp\left(-\frac{\varepsilon_h}{T_{h_2}}\right). \quad (1)$$

The parameter values have been adjusted in order to reproduce as best as possible the experimental data upon REB transport, yielding $\varepsilon_0 = 20\,\text{keV}$, $\alpha = 1$, $T_{h_1} = 100\,\text{keV}$, and $T_{h_2} = 12.5\,\text{MeV}$ [dashed red curve in Fig. 2-a)]. The corresponding fast electron mean energy over the $0.05 \le \varepsilon_h \le 20\,\text{MeV}$ range is $\bar{\varepsilon}_h = 1\,\text{MeV}$. The power law component of the electron spectrum, already observed in other kinetic simulations [23–26], significantly impacts K$_\alpha$ emission and must be taken into account to reproduce the experiment. This high sensitivity to the low energy part of the electron spectrum is due to the high collisional ionization rate of the inner shells for energies around a 100 keV [see for example the Sn K-shell ionization cross section [31], thin solid line in Fig. 2-a)].

To further validate the used REB source spectrum, we also set up at 45° from the target normal a X-ray spectrometer measuring in the $10\,\text{keV} < E_X < 3\,\text{MeV}$ range, relevant for the bremsstrahlung produced by the low energy part of the REB spectrum. The X-rays are detected by differential transmission on a stack of 15 successive metallic filters and 15 imaging plates (IP) [27]. The de-convolved detected X-ray spectrum is of the shape $F(E_X) = a.\exp(-E_X/T_1) + b.\exp(-E_X/T_2)$ with the parameters $a = (1.4 \pm 0.6) \times 10^4$, $T_1 = (22 \pm 2)$ keV, $b = (4 \pm 0.8) \times 10^3$ and $T_2 = (240 \pm 40)$ keV [blue curve on Fig. 2-b)]. The consistency of the analysis is confirmed by Monte Carlo (MC) simulations of the spectrometer, using the MCNPX code [28]. Because the bremsstrahlung emissions are not included in the hybrid code used to calculate the REB resistive transport [29] (see further below), the REB propagation in the targets, injected with the energy distribution of Eq. 1, was also calculated by MC simulations: The generated bremsstrahlung emission at 45° agrees with the measured photon spectrum (dashed red curve), validating the considered REB source. It is worth noting that T_1 and T_2 are of the order of the temperature T_{h_1} characterizing the lower energy part of the REB spectrum. A permanent magnet spectrometer set up at 64° from the target normal measured the energy distribution of electrons leaving the target in the range of 1 to 10 MeV, measuring a $T_h \sim 1.3$ MeV higher energy component, in very good agreement with the electron spectrum at the rear side of the simulated targets.

The REB transport through the multi-layer targets was simulated with a 2D axis-symmetric hybrid code [29] using, as initial density and temperature, the profiles extracted from the hydrodynamic simulations at the corresponding SP injection time. We considered a laser energy of 115 J and an adjustable absorption into the injected REB $\eta_{\text{laser}\to\text{e}}$ from 20 to 40% [30]. Transport simulations were run up to 8 ps in a 300 μm-radius simulation box, with 1 fs and 0.25 μm temporal and spatial resolutions respectively. Electrical resistivity is computed using the Drude model $\eta = m_e\nu/e^2 n_e$, with n_e the electron density and ν the electron collision frequency calculated with the Eidmann-Chimier model [14, 15], which takes into account electron-phonon (e-ph), electron-electron (e-e) and electron-ion (e-i) collisions according to the background density and temperature. A module based on Hombourger's cross sections [31] was used to calculate K$_\alpha$ absolute yields and size for comparison with experimental values.

The careful description of the energy, angular and spatial distributions of the REB source, as inspected from the PIC simulation results, resulted in a very good reproduction of the experimental Cu-K$_\alpha$ spot size as well as the absolute K$_\alpha$ yields. Open symbols in Fig. 1-a) show the simulation results for the Sn-K$_\alpha$ yield using

$\eta_{\mathrm{laser}\to\mathrm{e}} = 25\%$. The light blue shaded area indicates the yields obtained for $\pm 5\%$ variation of this parameter. The experimental Sn-K_α/Ag-K_α yield ratios as a function of the Al-sample areal density ρL [full symbols in Fig. 1-b)] are nicely reproduced by the transport simulations (open symbols, using $\eta_{\mathrm{laser}\to\mathrm{e}} = 25\%$). As explained above, the steeper ratio reduction in the compressed case is unambiguously associated with an increase of resistive energy losses in warm Al. This is obvious on the simulation results, a bit less for the experimental points but the effect of the different resistivity is quite clear for the thickest target data. From this set of benchmarked results, averaging over the simulation time and over a $50\,\mu$m radius around the REB propagation axis, we estimated the REB current density entering the Al-samples to be $\bar{j}_h \simeq 2.4 \times 10^{11}\,\mathrm{A.cm^{-2}}$.

Fig. 3-b) presents 2D maps of collisional and resistive energy losses per unit mass, time-integrated up to $t_1 = 2.1\,$ps after REB injection time, for solid (top) and compressed (bottom) targets, calculated with the hybrid code for targets with $L_0 = 80\,\mu$m. Comparing the two cases, and focusing on the Al sample (delimited by the vertical dashed lines) we clearly see that the collisional losses against target depth do not change while the resistive losses increase in terms of both yield and range. This is related to higher resistivity in the regions beyond the shock front. While the collisional losses extend over the entire target due to multiple diffusions, the resistive losses are confined into a more restricted volume around the REB propagation axis, where the current density is the highest. Fig. 4-a) shows the integration of the energy losses over the samples, for the two sample types, warm-dense (open symbols) and cold-solid (solid), as a function of the areal density ρL. While the trends for the collisional losses (green squares) are, as expected, fairly the same, the resistive losses (orange triangles) become progressively greater in warm samples compared to cold ones. Beyond $\rho L \sim 10.6\,\mathrm{mg.cm^{-2}}$ [vertical dashed line in Fig. 4-a)], they saturate due to the decrease of j_h after a certain target depth. Whole beam average collisional vs. resistive stopping cross sections taken at $\rho L_0 = 10.62\,\mathrm{mg.cm^{-2}}$ (solid) and $\rho L = 10.49\,\mathrm{mg.cm^{-2}}$ (compressed) yield 92 ± 17 vs. $67 \pm 20\,\mathrm{J.cm^2.g^{-1}}$ in cold-solid Al and 92 ± 17 vs. $80 \pm 20\,\mathrm{J.cm^2.g^{-1}}$ in warm-dense Al. By multiplying these results by the sample average density, and by normalizing to the number of fast electrons at the beginning of the sample, the resistive stopping powers in cold-solid and warm-compressed aluminum are 2.5 ± 0.7 vs. $5.4 \pm 1\,\mathrm{keV}/\mu$m. Fig. 4-b) presents the resistivity in cold-solid (squares) and warm-compressed (circles) Al, as well as the current density (triangles), averaged over the first $35\,\mu$m of the Al sample, plotted against time (and hence temperature). One can see that the ratio of the resistivities between warm-dense and cold-solid Al sample before the propagation of the fast electron beam, equal to 6.2, is clearly higher than the ratios of the given resistive stopping cross sections ($\simeq 1.2$) and of the resistive stopping powers ($\simeq 2.1$). The discrepancy highlights the time evolution of the resistivity in both warm and cold samples due to REB energy deposition. That non-monotonic behavior is the signature of the transition between a regime ruled successively by e-ph, e-e and e-i collisions in the solid case, and successively by e-e and e-i collisions in the compressed case [32]. The heating time needed to reach the Spitzer regime is considerably smaller than the REB duration for the smaller ρL samples, explaining why in this case [see Figs. 1-b) and 4-a)] the effects of higher initial η are less visible.

In conclusion, we characterized the collisional and resistive energy losses of REB transport at current densities exceeding $10^{11}\,\mathrm{A.cm^{-2}}$ in both cold-solid and warm-dense Al at twice solid density. The absolute K_α yield measurements linked to the total number of transported fast electrons are reproduced by a detailed simulation suite. The obtained values of the stopping cross section and stopping power corroborate our previous analytical and numerical predictions [32]. At lower REB current density, $\bar{j}_h \approx 8 \times 10^{10}\,\mathrm{A.cm^{-2}}$ (time-average), the energy losses were dominated by the direct collisions with the background material [26, 32]. Our data and simulations unravel the role of resistive losses in REB transport, linked to the target resistivity, both the initial difference due to shock-induced heating yielding higher e-e collision frequency, and its ps-scale transient behavior during REB energy deposition. The first hundreds of fs of transport can indeed play a determinant role on the generation of resistive magnetic fields, partially conditioning the subsequent beam profile characteristics [34, 35]. The transition to warm dense states is FI-relevant because of the understanding of REB transport in high resistive regions such as the cone tip material and just beyond it and of the benchmarking of transport simulations extendable to the full-scale FI conditions.

We gratefully acknowledge the support of the Jupiter Laser Facility (LLNL) staff during the experimental run, and Alphanov for the laser-cutting of the targets. This work was performed through funding from the Conseil Régional d'Aquitaine, project PETRA 2008 13 04 005, and both the French National Agency for Research (ANR) and the competitiveness cluster Alpha - Route des Lasers, project TERRE ANR-2011-BS04-014, and in the framework of the Investments for the future Programme IdEx Bordeaux LAPHIA (ANR-10-IDEX-03-02). The numerical study was supported by Grant No. ENE2009-11668 of the Spanish Ministry of Education and Research and by the European Science Foundation SILMI program, and used HPC resources from CeSViMa and from GENCI-CINES (Grants No. 2011-056129 and No. 2012-056129). RJG and PM were supported by EPSRC (grant number EP/J003832/1). This work has been carried out within the framework of the EUROfusion Consortium and has received funding from the European Union′s Horizon 2020 research and innovation program under grant agreement number 633053. The views and opinions expressed herein do not necessarily reflect those

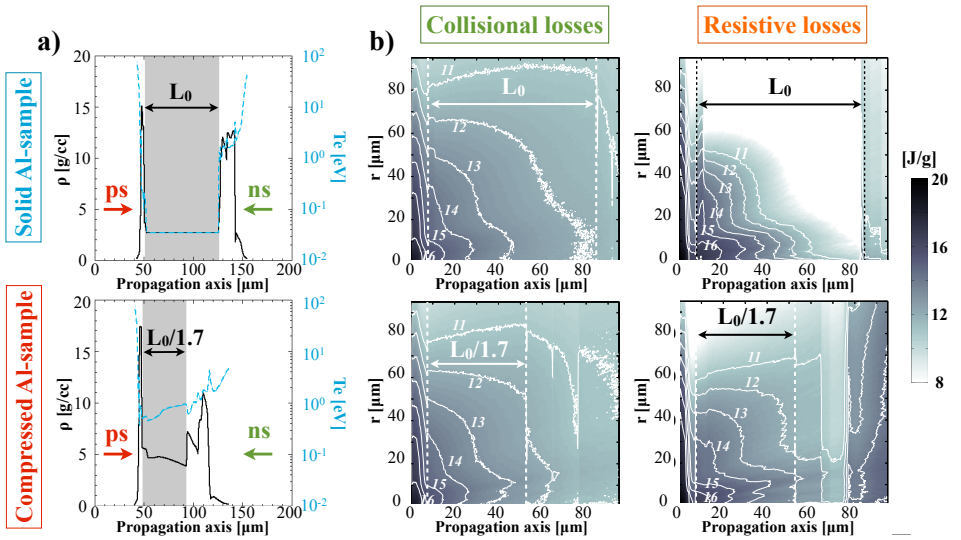

FIG. 3. (color online) **(a)** Hydrodynamic simulation results for the density and temperature axis profiles at the SP injection time (focused on the left hand side), in the Al-sample solid (top) and compressed (bottom) cases. **(b)** Corresponding REB transport simulation results of the time-integrated collisional (left hand-side plots) and resistive (right hand-side plots) REB energy loss per unit mass (in logarithmic scale), extracted 2.1 ps after REB injection. All the figures correspond to the thickest targets ($L_0 = 80\,\mu$m).

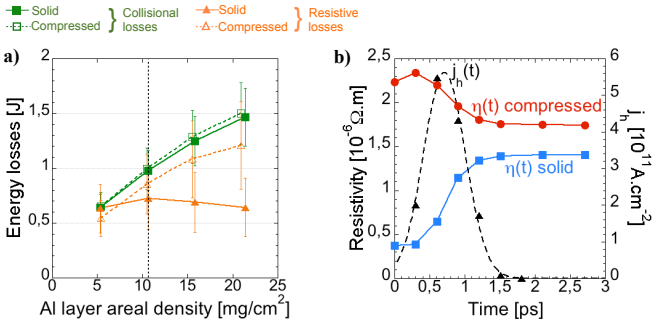

FIG. 4. (color online) Results from the hybrid transport simulations assuming $\eta_{\mathrm{laser}\to\mathrm{e}} = 25\%$: **(a)** Time-integrated collisional (green squares) and resistive (orange triangles) energy losses in solid (full symbols) and compressed (open symbols) Al-samples, as a function of their areal density ρL. **(b)** Time evolution of the resistivity of cold-solid (blue squares) and of warm-compressed (red circles) Al samples, as well as the current beam density (black triangles) averaged over a thickness of $L = 35\ \mu$m and a radius of 25 μm around REB propagation axis, calculated from hybrid simulations.

of the European Commission.

[1] M. Tabak, J. Hammer, M. E. Glinsky, W.L. Kruer, S.C. Wilks, J. Woodworth, E.M. Campbell, M.D. Perry, and R.J. Mason, Phys. Plasmas **1**, 1626 (1994).

[2] R. Kodama *et al.*, Nature **412**, 798 (2001).

[3] S. Atzeni, A. Schiavi, C. Bellei, Phys. Plasmas **14**, 052702 (2007).

[4] S. Baton *et al.*, Phys. Plasmas **15**, 042706 (2008).

[5] J.J. Honrubia, and J. Meyer-ter-Vehn, Plasma Phys. Control. Fusion **51**, 014008 (2009).

[6] A.A. Solodov, K. S. Anderson, R. Betti, V. Gotcheva, J. Myatt, J. A. Delettrez, S. Skupsky, W. Theobald, and C. Stoeckl, Phys. Plasmas **16**, 056309 (2007).

[7] A. Debayle, J. J. Honrubia, E. d'Humières, and V. T. Tikhonchuk, Plasma Phys. Control. Fusion **52**, 124024 (2010).

[8] A. J. Kemp and L. Divol, Phys. Rev. Lett. **109**, 195005

(2012).
[9] International Commission on Radiation Units and Measurements, Stopping powers for electrons and positrons, Technical Report 37, Bethesda, MD, USA (1984).
[10] V.T. Tikhonchuk, Phys. Plasmas **9**, 1416 (2002).
[11] A.J. Kemp, Y. Sentoku, V. Sotnikov, and S.C. Wilks, Phys. Rev. Lett. **97**, 235001 (2006).
[12] P. Norreys *et al.*, Nucl. Fusion **54**, 054004 (2014).
[13] J.J. Santos *et al.*, J. Plasma Physics **79**, 429 (2013).
[14] K. Eidmann, J. Meyer-ter-Vehn, T. Schlegel, and S. Huller, Phys. Rev E **62**, 1202 (2000).
[15] B. Chimier, V.T. Tikhonchuk, and L. Hallo, Phys. Rev B **75**, 195124 (2007).
[16] A.G. MacPhee *et al.*, Phys. Plasmas **79**, 10F302 (2008)
[17] S. Le Pape *et al.*, Opt. Lett. **34**, 2997 (2009).
[18] P.-H. Maire, R. Abgrall, J. Breil, and J. Ovadia, SIAM J. Sci. Comput. **29**, 1781 (2007).
[19] R.B. Stephens *et al.*, Phys. Rev E **69**, 066414 (2007).
[20] H. Friesen *et al.*, Phys. Plasmas **84**, 023704 (2013).
[21] J.F. Seely, L.T. Hudson, G.E. Holland, and A. Henins, Appl. Opt. **47**, 2767 (2008).
[22] D.R. Welch, D.V. Rose, R.E. CLark, T.C. Genoni, and T.P. Hughes, Comp. Phys. Comm. **164**, 183188 (2004)
[23] S. Micheau, A. Debayle, E. d'Humières, J.J. Honrubia, B. Qiao, M. Zepf, M. Borghesi, and M. Geissler, Phys. Plasmas **17**, 122703 (2010).
[24] C. Ren, M. Tzoufras, F.S. Tsung, W.B. Mori, S. Amorini, R.A. Fonseca, L.O. Silva, J.C. Adam, and A. Heron, Phys. Rev. Lett. **93**, 185004 (2004).
[25] A. Debayle, J.J. Honrubia, E. d'Humières, and V.T. Tikhonchuk, Plasma Phys. Control. Fusion **52**, 124024 (2010).
[26] B. Vauzour *et al.*, Phys. Rev. Lett. **109**, 255002 (2012).
[27] C.D. Chen *et al.*, Rev Sci. Instrum. **79**, 10E305 (2008).
[28] D. Pelowitz, MCNPX user's manual version 2.7.0 (2011).
[29] J.J. Honrubia, C. Alfonsín, L. Alonso, B. Pérez, and J.A. Cerrada, Laser Part. Beams **24**, 217 (2006).
[30] B. Westover *et al.*, Phys. Plasmas **18**, 063101 (2011).
[31] C. Hombourger, J. Phys. B **31**, 3693 (1998).
[32] B. Vauzour *et al.*, Phys. Plasmas **21**, 033101 (2014).
[33] L. Spitzer, Physics of Fully Ionized Gases (1962).
[34] R.H.H. Scott *et al.*, Phys. Rev. Lett. **109**, 015001 (2011)
[35] D.A. MacLellan *et al.*, Phys. Rev. Lett. **111**, 095001 (2013)